Synthesis of iron(III)-carbonyl complex with variable wavelength range for CO release depending on protonation and deprotonation of axial phosphorous ligands

Synthesis of iron(III)-carbonyl complex with variable wavelength range for CO release depending on protonation and deprotonation of axial phosphorous ligands

Seiya Tanaka, Natsuo Nomura, Takanori Nishioka, Masakazu Hirotsu, Hiroshi Nakajima

Synthesis of iron(III)-carbonyl complex with variable wavelength range for CO release depending on protonation and deprotonation of axial phosphorous ligands

Seiya Tanaka,[a] Natsuo Nomura,[a] Takanori Nishioka,[a] Masakazu Hirotsu,[b] and Hiroshi Nakajima[a,] *

[a]Division of Molecular Materials Science, Graduate School of Science, Osaka City University, 3-3-138 Sugimoto, Sumiyoshi-ku, Osaka, 558–8585, Japan.

[b]Department of Chemistry, Faculty of Science, Kanagawa University, 2946, Tsuchiya, Hiratsuka-shi, Kanagawa, 259-1293, Japan.

ABSTRACT N,C,S-pincer iron(III) carbonyl complexes with two phosphorus ligands—*trans*-[Fe(L-κ^3*N,C,S*)(CO)(PR_3)$_2$]PF_6 ([**1**]PF_6, R = Me; [**2**]PF_6, R = OEt) are light-inducible CO releasers under ambient conditions. Optical wavelength ranges corresponding to such a CO release depend on the phosphorous ligands. Complex [**1**]PF_6 responds to light with wavelengths shorter than 500 nm, while the photosensitivity of [**2**]PF_6 is extended to wavelengths up to 800 nm, reaching the so-called phototherapeutic window. Theoretical and experimental studies suggest that the electron-donating ability of phosphorous ligands is essential to determine the wavelength range corresponding to photo-CO dissociation, although the steric difference in the phosphorous ligands for [**1**]PF_6 and [**2**]PF_6 hampers the exclusive evaluation of the electronic effect for CO dissociation from such complexes. A newly synthesized N,C,S-pincer iron(III) carbonyl complex with 1,3,5-triaza-7-phosphaadamantane (PTA) as axial ligands ([**3**]PF_6) has shown variable photosensitivity for the dissociation of CO in response to protonation of the PTA ligand. Based on this finding, in the present study, [**3**]PF_6 is used to confirm the photo-CO dissociation mechanism proposed for [**1**]PF_6 and [**2**]PF_6 and provide clues to molecular design for adjusting the ranges of optical wavelengths required for CO dissociation from *trans*-[Fe(PyBPT-κ^3*N,C,S*)(CO)(PR_3)$_2$]PF_6.

1. Introduction

Carbon monoxide (CO) is a colorless and odorless gas that is mainly produced by the incomplete combustion of hydrocarbon materials and has been recognized as a toxic molecule.[1, 2] The strong affinity of CO with the iron center of heme leads to the formation of carboxyhemoglobin (COHb), which inhibits oxygen-transportation in blood.[3] In cells, CO impairs the function of cytochrome *c* oxidase and blocks the aerobic respiratory chain. In general, toxic symptoms such as headache, shortness of breath and dizziness occur at the 10 - 30% COHb level in the blood, and fatal consequences are caused at higher COHb levels (> 50%).[3] Meanwhile, for decades, studies of CO have focused on its physiological role in mammalian cells. Heme oxygenase produces endogenous CO in the heme metabolic pathway. The CO produced acts as a gasotransmitter like nitric oxide or hydrogen sulfide,[4-7] and participates in many biological events, such as respiration, blood pressure regulation, immune control, and apoptosis through reactions with some mediators, which suggests a potential for the use of CO as a therapeutic agent. Studies of exogenous CO with animals have revealed cytoprotective functions, including anti-apoptosis, anti-inflammation effect, and anti-proliferative actions.[8, 9] However, the concentration of inhaled CO (250 - 500 ppm), which is essential for activating CO as a therapeutic agent,[9] risks toxic effects due to the lack of specific delivery to target organs. Thus, alternative materials for CO inhalation, which are referred to as CO-releasing molecules CORM, are required for developing the therapeutic effects of CO as a medicine.[10-12]

Metal carbonyl complexes, which are generally composed of a transition metal, CO and ancillary ligands, are expected to be potential CORMs.[12-14] Metal carbonyl complexes that progressively release CO in the course of their hydrolysis allow for CO administration at a lower concentration than the toxic level in blood.[15-17] The current goal of metal carbonyl CORMs is

specific CO release without toxic side effects, depending on external stimuli such as environmental molecules,[15] pH,[16, 17] and light.[12, 14, 18-20] Some metal carbonyl CORMs have been studied in cultured cell lines or animals to evaluate their therapeutic effects and biological toxicities.[10, 21, 22]

Photo-responsive CORMs (photoCORMs) are attractive materials, which release CO upon photo-irradiation of the molecules.[12, 14, 18-20] To achieve site-specific and time-independent administration of CO in the living body, photoCORMs should be stable in aqueous media under dark conditions and quickly release CO upon the irradiation of light within the photo-therapeutic window (wavelength range of λ = 600 - 900 nm).[23] The use of biometals is another criterion for designing metal carbonyl photoCORMs with high biocompatibility.[10, 21] Recently, manganese-carbonyl photoCORMs have been reported that are designed to acquire biocompatibility.[24-30] Iron-carbonyl complexes are another choice because of the higher permissible amount of iron ions in the body. Mammals possess iron regulatory systems that respond to an abundance of iron ions in the body.[31, 32] This reduces the risk of free iron ions being produced after CO release from CORMs.[33-35] The first reported iron-based photoCORM was CORM-S1, which consists of an iron(II)-dicarbonyl unit with an ancillary ligand cysteamine.[36] This complex achieved CO dissociation in response to visible light irradiation with an effective wavelength of up to 470 nm. The construction of an iron-based photoCORM responsive to longer-wavelength light has been achieved by using a combination of conservative iron(0) and iron(II) carbonyl complexes with near-IR sensitive materials.[37, 38] The exothermic reaction of materials by near-IR irradiation induces thermal degradation of the carbonyl complexes.[39, 40]

In a previous study, we reported iron(III) carbonyl complexes, *trans*-[Fe(PyBPT-κ^3*N,C,S*)(CO)$(PR_3)_2$]PF_6 ([**1**]PF_6, R = Me; [**2**]PF_6, R = OEt) as photoCORMs, where PyBPT is a doubly deprotonated form of 3'-(2''-pyridyl)-1,1'-biphenyl-2-thiol formed via the C-S bond cleavage of the dibenzothiophene derivative (Figure 1a).[41]

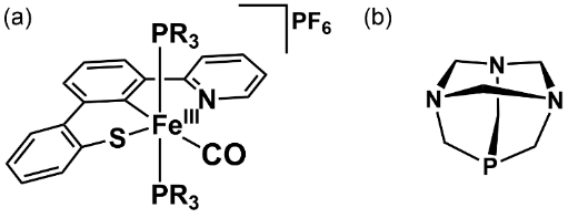

[**1**]PF_6, R = Me; [**2**]PF_6, R = OEt;
[**3**]PF_6, PR_3 = PTA

Figure 1. Molecular structures for (a) [**1**]PF_6 - [**3**]PF_6 and (b) 1,3,5-triaza-7-phosphaadamantane (PTA).

Complex [**1**]PF_6 releases CO in response to visible light (λ < 500 nm), and [**2**]PF_6 is sensitive to visible–near-IR light (λ < 800 nm). Experimental and theoretical analyses for the CO dissociation mechanism from [**1**]PF_6 and [**2**]PF_6 suggest two modes of photo-CO dissociation in both complexes: dπ-dσ* transition by visible light and dπ-dπ transition by near-IR light. These transitions lead to the depopulation of the π-bonding orbital of the Fe-CO bond and destabilize the coordination of CO, although the dπ-dπ transition is inefficient due to overlapping with strong ligand to metal charge transfer (LMCT) transition.[41] According to Tolman electronic parameters,[42, 43] the electron-donating ability of $P(OEt)_3$ to a metal atom is lower than PMe_3. The reduced electron donation from $P(OEt)_3$ to iron(III) in comparison to PMe_3 consequently attenuates the π-bonding of Fe-CO. This increases the sensitivity of [**2**]PF_6 to near-IR light for CO dissociation by the inefficient dπ-dπ transition. The controversial point of the mechanism laid in the different cone angles of the phosphorous ligands (118° for PMe_3 of [**1**]PF_6 and 109°

for $P(OEt)_3$ of [**2**]PF_6),[44] which raise different steric effects on the *cis*-arranged CO ligand and prevent a simple ascription of the Fe-CO bond attenuation to the electronic effects of the phosphorous ligands.

In this study, we synthesized a N,C,S-pincer iron(III) carbonyl complex [**3**]PF_6 with 1,3,5-triaza-7-phosphaadamantane (PTA,[45-47] Figure 1b) as axial ligands to elucidate the electronic effect of phosphorous ligands on CO dissociation in response to near-IR light irradiation. PTA is a cage-like water-soluble phosphine, which possesses a protonation site at an amino group with a pK_a value of ca. 6.[47] Experimental and theoretical studies have shown that additional protonation at residual amino groups is thermodynamically unfavorable since it changes the orbital hybridization of the nitrogen atoms and leads to distortion of the cage-like structure.[47] Meanwhile, previous studies have shown that single protonation of PTA is sufficient to modulate the electron density on the central metal of the metal-PTA complexes.[47] As the steric effect of single protonation of PTA on the coordination of the CO ligand is negligible, the comparative photoreaction of [**3**]PF_6 before and after protonation can allow for verifying the CO dissociation mechanism that distinguishes [**1**]PF_6 and [**2**]PF_6 in terms of sensitivity to near-IR light without considering the steric aspect of the axial phosphorous ligands.

2. Material and methods

2-1. Materials. All solvents and reagents were used as received. All solvents and reagents for synthesis were purchased from Kanto Chemical Co., Inc., FUJIFILM Wako Pure Chemical Industries, Ltd., Tokyo Chemical Industry Co., Ltd., Sigma-Aldrich, Nacalai Tesque, Inc., BLD Pharmatech Ltd., Ark Pharm, Inc, and Santa Cruz Biotechnology, Inc. The [{Fe(μ-PyBPT-

κ^3*N,C,S*)$(CO)_2$}Fe$(CO)_3$] complex, which is the precursor of complexes **1**, **2**, and **3**, was prepared by a literature procedure.[48]

2-2. Spectroscopy and spectrometry. All spectroscopy and spectrometry were performed under ambient conditions unless otherwise noticed. NMR spectra were recorded by using a Bruker AVANCE 300 FT-NMR spectrometer (Bruker Japan Co.) at room temperature. IR spectra were recorded with a JASCO FT/IR-4600 type A (Jasco Co.) equipped with an attenuated total reflection (ATR) unit. Electronic absorption spectra were recorded by a HITACHI UH4150 (Hitachi Co.). EPR spectra were recorded by a Bruker Biospin Elexsys E500 spectrometer (Bruker Japan Co.). Mass spectra were recorded by an Applied Biosystems Mariner time-of-flight mass spectrometer (Thermo Fisher Scientific Co.).

2-3. Electrochemistry. Cyclic voltammetry was performed with an ALS600A electrochemical analyzer (BAS Co.) under an N_2 atmosphere at room temperature in the dark. The working, reference, and counter electrodes were a glassy carbon disk electrode with a diameter of 3 mm, a reference Ag/Ag^+ (0.01 M $AgNO_3$) and a platinum wire, respectively. The electrolysis solution of CH_2Cl_2 contained 1.1 mM sample complex and 0.1 M $^nBu_4NPF_6$ as a supporting electrolyte. The electrode potentials were corrected using the redox potential of ferrocene/ferrocenium $E^{\circ\prime}$ (Fc/Fc^+).

2-4. Synthesis of *trans*-[Fe^{II}(PyBPT-κ^3*N,C,S*)(CO)$(PTA)_2$] (3). [{Fe(μ-PyBPT-κ^3*N,C,S*)$(CO)_2$}Fe$(CO)_3$] (102 mg, 1.9×10^{-4} mol) and PTA(131 mg, 8.3×10^{-4} mol) were placed in a Schlenk tube with a Teflon valve and dissolved in dehydrated THF (10 mL). The solution was then stirred at 70 ºC for 3 h under an N_2 atmosphere to obtain an orange suspension. The precipitate was filtered under reduced pressure, and the filtrate was evaporated to dryness. The orange residue was suspended in ice-cold *n*-hexane and collected by filtration. The collected

solid was recrystallized in CH_2Cl_2/cyclohexane = 1 : 10 (v/v) at 0 ºC to produce fine crystals, which were collected by decantation, washed with THF, and dried in vacuo (137 mg, 2.1×10^{-4} mol, 93%). The product was stored under ambient conditions until use.

A single crystal suitable for X-ray crystallography was obtained by recrystallization with CH_2Cl_2/toluene/*n*-hexane = 1 : 1 : 4 at 0 ºC. ^{1}H NMR (300 MHz, C_6D_6): δ 3.43 (d, 1H, $^2J_{HH}$ = 15.6 Hz, PTA), 3.56 (d, 1H, $^2J_{HH}$ = 15.1 Hz, PTA), 3.70 (d, 1H, $^2J_{HH}$ = 12.8 Hz, PTA), 3.90 (d, 1H, $^2J_{HH}$ = 12.5 Hz, PTA), 6.04 (ddd, 1H, $^3J_{HH}$ = 5.7, 7.3 Hz, $^4J_{HH}$ = 1.4 Hz, 5-py), 6.74 (t, 1H, $^3J_{HH}$ = 7.5 Hz, 4-py), 6.89 (ddd, 1H, $^3J_{HH}$ = 7.2, 7.5 Hz, $^4J_{HH}$ = 1.6 Hz, 4-BPT), 6.97 (ddd, 1H, $^3J_{HH}$ = 7.2, 7.8 Hz, $^4J_{HH}$ = 1.6 Hz, 5-BPT), 7.07 (d, 1H, $^3J_{HH}$ = 7.9 Hz, 3-py), 7.21 (tt, 1H, $^3J_{HH}$ = 7.7 Hz, J_{PH} = 1.3 Hz, 5′-BPT), 7.48 (dd, 1H, $^3J_{HH}$ = 7.7 Hz, $^4J_{HH}$ = 1.0 Hz, 4′-BPT), 7.60 (dd, 1H, $^3J_{HH}$ = 7.7 Hz, $^4J_{HH}$ = 1.4 Hz, 6-BPT), 7.87 (d, 1H, $^3J_{HH}$ = 7.6 Hz, 6′-BPT), 8.02 (dd, 1H, $^3J_{HH}$ = 7.7 Hz, $^4J_{HH}$ = 1.6 Hz, 3-BPT) 8.51 (d, 1H, $^3J_{HH}$ = 5.6 Hz, 6-py). ^{31}P{^{1}H} NMR (121 MHz, C_6D_6) : δ −32.4. IR (KBr): ν_{CO} = 1908 cm^{-1}. Anal. Calcd for **3** ($C_{30}H_{35}FeN_7OP_2S$): C, 54.63; H, 5.36; N, 14.87. Found: C, 54.23; H, 5.41; N, 14.59.

2-5. Synthesis of *trans*-[Fe^{III}(PyBPT-κ^3*N,C,S*)(CO)(PTA)$_2$]PF$_6$ ([3]PF$_6$). Tris(4-tolyl)aminium hexafluorophosphate (113 mg, 2.7×10^{-4} mol) was mixed with **3** (100 mg, 1.5×10^{-4} mol) in CH_2Cl_2 (20 mL) in the dark. The reaction mixture was stirred at room temperature for 1 h, followed by the addition of toluene (10 mL). After removing the solvent to a minimum volume under reduced pressure, the suspension was filtered to collect a dark greenish-blue powder, which was rinsed with toluene and dried in vacuo (83 mg, 1.0×10^{-4} mol, 68%). The mass spectrum for the product was consistent with the composition formula of [**3**]$^+$ (Figure S1). The product was stored in the dark under ambient conditions until use.

2-6. Photoreaction of [3]PF_6 and [3H$^+$]PF_6. A 0.24 mM CH_2Cl_2 solution of the complex placed in a 1 cm^2 square optical cell (1 mL) was irradiated with a monochrome light (λ = 400 - 800 nm) generated by a fluorescent spectrometer (HITACHI F-7000 fluorescence spectrometer, Hitachi Co.) in the dark. A UV light cut filter was used to remove light diffracted at a higher order of the incident light from the monochrome light before irradiating the sample solution. The photon flux density (/mol·s^{-1}·m^{-2}) at each wavelength adopted in this study was calculated from the optical power density measured on the surface of the sample cell using a pyranometer (ML-01, EKO Instruments Co.) with an effective spectral range of 400-1100 nm (Figure S11). UV-Vis spectra for the reaction solution were recorded every 15 min to 30 min during irradiation. The photolytic kinetics was traced by changes in absorbance at 600 and 612 nm for [**3**]PF_6 and [**3**H$^+$]PF_6, respectively. Photolysis plots were obtained as the average of three independent experiments and analyzed by the first-order kinetic equation.

2-7. Computational Details. The structures of complexes **3**, [**3**]$^+$, and [**3**H$^+$]$^+$ were optimized by DFT calculations using the Gaussian 09 program package.[49] The crystal structure of **3** was used as the initial model of **3**, [**3**]$^+$, and [**3**H$^+$]$^+$. The rB3LYP (**3**) and uB3LYP ([**3**]$^+$ and [**3**H$^+$]$^+$) density functional methods and the 6-311+G(d,p) basis set were used for the calculations. Optimized structures for **3**, [**3**]$^+$, and [**3**H$^+$]$^+$ are shown in Figure S12. The selected bond distances and angles for the complexes are shown in Table S1, and the molecular coordinates are listed in Tables S2-S4. Harmonic vibrational frequencies were calculated for the optimized geometries using the 6-311G(d,p) level.

Time-dependent DFT calculations for [**3**]$^+$ and [**3**H$^+$]$^+$ were performed using the optimized structures at the uB3LYP/6-311+G(d,p) level. Electronic excitations and the related molecular

orbitals are given in Tables S7 and S5 for [**3**]$^+$ and Tables S8 and S6 for [**3**H$^+$]$^+$, respectively. Selected Mulliken atomic spin densities for [**3**]$^+$ and [**3**H$^+$]$^+$ are shown in Table S9.

2-8. X-ray Crystallography. Diffraction data for **3** was collected by using a Rigaku AFC11/Saturn 724+ CCD diffractometer with monochromated Mo-Kα radiation (λ = 0.710747 Å) (Rigaku Co.). The data were processed and corrected for Lorentz and polarization effects using the CrystalClear software package. The analyses were carried out using the WinGX software.[50] Absorption corrections were applied using the MultiScan method. The structures were solved using direct methods (SIR97)[51] and refined by full-matrix least-squares with F^2 using SHELXL-2018/3.[52] Crystallographic data are summarized in Table S10. Non-hydrogen atoms were refined anisotropically. Hydrogen atoms were located in a difference Fourier map and isotopically refined.

3. Results and discussion

3-1. Synthesis of N,C,S-pincer iron(II/III) carbonyl complex with PTA ligand. The synthesis of *trans*-[Fe(PyBPT-κ^3*N,C,S*)(CO)(PTA)$_2$] (**3**) was achieved in analogy with the synthesis of **1** and **2**.[41] . Simple replacement of PMe_3 of **1** with PTA in synthetic procedures provided **3**. Complexes **1** - **3** are the one-electron reduced forms and synthetic sources of [**1**]PF_6 - [**3**]PF_6, respectively. The assignment of the ^{1}H NMR signals for **3** in C_6D_6 was carried out in comparison with the spectra obtained for [{Fe(μ-PyBPT-κ^3*N,C,S*)(CO)$_2$}Fe(CO)$_3$] [48] and intact PTA (Figure S2). Signals at 6.05-8.52 ppm were assigned to the protons of PyBPT. The ^{31}P{^{1}H} NMR spectrum for **3** in C_6D_6 showed a single signal at -32.4 ppm, which was similar to that observed for PMe_3 of **1** [41] and confirmed that the PTA ligands were bound to the central iron

(Figure S3). The single signal suggested that the coordination spheres of the two PTA ligands were equivalent in solution.[41]

A crystal structure of **3** obtained by X-ray analysis is depicted in Figure 2.

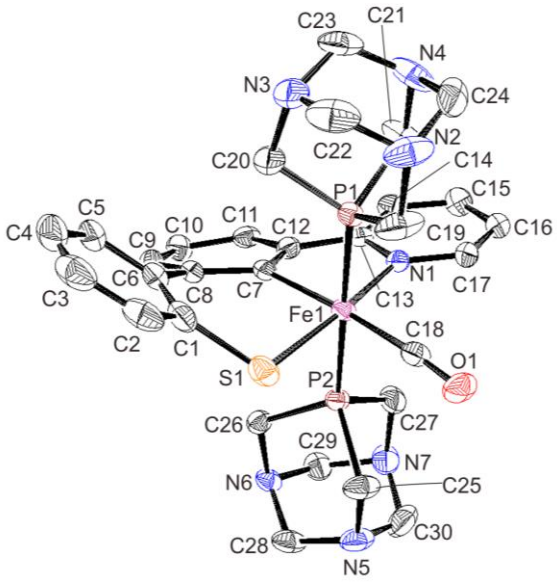

Figure 2. ORTEP drawing of **3** with thermal ellipsoids at the 50% probability level. Hydrogen atoms are omitted for clarity.

Selected bond distances and angles for **3** are listed in Table 1. Corresponding data for **1** and **2** are reproduced in the same table for comparison.[41] The overall conformation of **3** was similar to those of **1** and **2**,[41] except for a larger bending of the equatorial tridentate ligand at the thiophenol ring. As with cases **1** and **2**, the structural variance in the crystal and NMR data implied a quick flip-flop motion of the equatorial ligand in solution.[41] The mean Fe-P distances followed the order of 2.243 Å (**1**, PMe_3) > 2.223 Å (**3**, PTA) > 2.206 Å (**2**, $P(OEt)_3$), which was reversed between **3** and **2** in terms of the steric bulk of the ligands estimated from the Tolman cone angles (118° (**1**, PMe_3) > 109° (**2**, $P(OEt)_3$) > 103° (**3**, PTA)).[44, 47] The more bent shape of the equatorial ligand observed in the crystal structure of **3** is a possible cause of

larger steric hindrance, which prevents the PTA ligands from approaching more closely the central iron despite the smaller cone angle compared to $P(OEt)_3$.

Complex	**3**	**1**[a]	**2**[a]
Fe1–S1	2.2944(18)	2.2777(7)	2.2915(10)
Fe1–C7	2.013(5)	1.997(2)	2.005(3)
Fe1–N1	1.991(4)	1.9799(19)	1.989(3)
Fe1–C18	1.785(5)	1.761(2)	1.773(4)
Fe1–P1	2.2242(17)	2.2511(8)	2.2193(10)
Fe1–P2	2.2208(16)	2.2340(8)	2.1924(10)
C18–O1	1.144(7)	1.161(3)	1.156(4)
Fe1–C18–O1	174.6(5)	176.2(2)	178.2(3)
N1–Fe1–S1	172.08(12)	175.97(6)	171.16(8)
C7–Fe1–C18	175.2(5)	178.46(10)	178.05(15)
P1–Fe1–P2	179.40(6)	174.68(3)	179.27(4)
Fe1–S1–C1–C6	38.5(5)	14.1(2)	29.6(3)
Interplanar angle [b]	28.8(5)	22.46(5)	27.08(10)
Interplanar angle [c]	10.6(5)	7.83(4)	6.26(15)

Table 1. Selected bond lengths (Å) and angles (deg) for **3**. [a]Reproduced from ref. 41.

Alternatively, the stronger π-electron acceptance of $P(OEt)_3$ from the central iron in comparison to the other phosphine ligands may be a dominant determiner of the shorter Fe-P bond. The P-O anti-bonding component in the phosphite ligand was more effective than the P-C anti-bonding component in phosphine ligands to accept electrons through Fe-P π-backbonding (*vide infra*).

3-2. One-electron oxidation and single protonation of complex 3. The one-electron oxidation of **3** to form $[\mathbf{3}]^+$, in which the central iron ion is formally trivalent, was achieved by reaction with $N(4\text{-tolyl})_3PF_6$ in CH_2Cl_2 in the dark. From UV-Vis spectroscopy, **3** showed progressive

changes with isosbestic points until an equimolar amount of the oxidant was added (Figure S4). The purified [**3**]$^+$ species ([**3**]PF_6) was available by precipitation from toluene. The mass spectrum of the purified product showed no changes in the structural components of **3** after the oxidation (Figure S1). The UV-Vis spectra measured for **3** and [**3**]PF_6 in CH_2Cl_2 are shown in Figure 3.

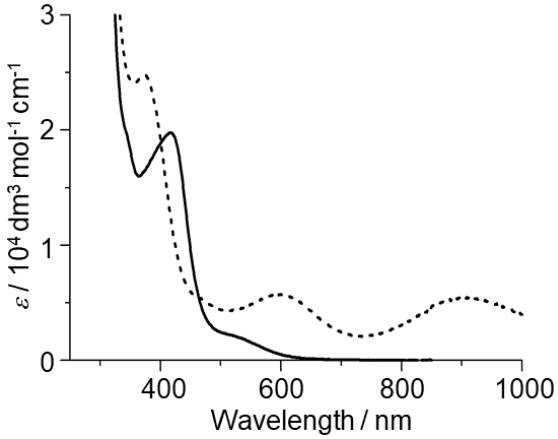

Figure 3. UV-Vis spectra for **3** (—) and [**3**]PF_6 (----) dissolved in CH_2Cl_2.

The spectral features observed for **3** and [**3**]PF_6 are similar to those found for **1**, **2**, and their oxidized forms ([**1**]PF_6 and [**2**]PF_6), respectively.[41] The charge-transfer bands of **3**, including the metal-to-ligand and intra-ligand were observed at 420 nm (417 and 408 nm for **1** and **2**, respectively). The shoulder of **3** at 530 nm is also assignable to charge transfer transitions (550 and 510 nm for **1** and **2**, respectively). Absorption bands characteristic of the one-electron oxidation product are observed at 600 nm and 904 nm (573, 853 nm for [**1**]PF_6 and 581, 813 nm for [**2**]PF_6, respectively), which are predominantly ascribed to the LMCT transitions.[53, 54]

The EPR spectrum for [**3**]PF_6 showed an isotropic triplet signal at g_{iso} = 2.043 with a hyperfine coupling constant (A_{iso}) = 1.73 mT at room temperature (Figure S5). The triple splitting was attributed to an unpaired electron of the central iron equivalently delocalized to the phosphorous

atoms of the two PTA ligands. A larger A_{iso} value was obtained for [**2**]PF_6 (g_{iso} = 2.038; A_{iso} = 2.4 mT).[41] This accords with the theoretical data in a previous report, which suggested that the P-O anti-bonding component in the phosphite ligand is more favorable than the P-C anti-bonding component in the phosphine ligands to accept electrons from the central iron through Fe-P π-backbonding.[41] The larger A_{iso} value of [**3**]PF_6 compared to [**1**]PF_6 (g_{iso} = 2.044; A_{iso} = 1.4 mT)[41] indicated that PTA is more effective than PMe_3 in accepting electrons from the central iron among the phosphine ligands.

Table 2 compares the vibrational energies of the C-O stretching modes (ν_{CO}) of the carbonyl ligands in **3** and [**3**]PF_6 with those in **1**, **2** and their oxidized forms. The IR spectra obtained for **3** and [**3**]PF_6 are shown in Figures S6a and c.

3	[**3**]PF_6	**3**H^+	[**3**H^+]PF_6	**1**	[**1**]PF_6	**2**	[**2**]PF_6
1908	1992	1929	2015	1891	1983	1922	2011

Table 2. The ν_{CO} energies (cm^{-1}) for **3**, [**3**]PF_6, and the protonated forms. The corresponding data for complexes **1** and **2** are reproduced for comparison.[41]

The upward shifts in the ν_{CO} energies observed for the corresponding oxidized forms are attributed to the reduced π-backbonding to the carbonyl ligands due to removing an electron from the central iron atoms. The IR data suggested that the electron-donating ability of the phosphorous ligands immediately affected the π-backbonding. The orders of the ν_{CO} energies for **1 - 3** and for [**1**]PF_6 - [**3**]PF_6 were consistent with the Tolman electronic parameters for PMe_3 (2064 cm^{-1}), $P(OEt)_3$ (2076), and PTA (2069).[44, 55] One-electron oxidation led to upward shifts of ca. 90 cm^{-1} regardless of the axial phosphorous ligands.

Free PTA accepts a single proton at one of the three amino groups with a pK_a of ca. 6.[47] Experimental and theoretical studies have shown that the further protonation of mono-protonated PTA is thermodynamically unfavorable due to steric disorder in the amino groups generated by an alteration in the hybridized orbital of nitrogen atoms.[47] This is also true for **3** and [**3**]PF_6. When an equimolar amount of CF_3SO_3H was added as a proton source, the UV-Vis spectrum of **3** in CH_2Cl_2 showed a quick band shift from 432 nm to 390 nm (Figure 4), and further addition of CF_3SO_3H led to no changes in the spectrum.

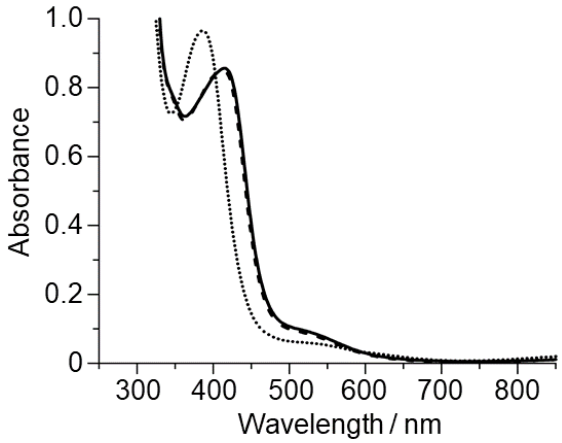

Figure 4. UV-Vis spectra of **3** (—) dissolved in CH_2Cl_2; (····) after the addition of 1.1 eq. of CF_3SO_3H; (– –) after the subsequent addition of an equimolar amount of Me_4NOH.

Subsequent addition of Me_4NOH restored the band to the original wavelength, confirming that the reaction with CF_3SO_3H was a reversible protonation reaction. Likewise, [**3**]PF_6 showed spectral changes, depending on the amount of CF_3SO_3H added until reaching the equimolar amount of the complex (Figure 5), while additional CF_3SO_3H over the equimolar amount did not show productive changes in the spectrum, except for the gradual diminishment of the characteristic bands of [**3**]PF_6.

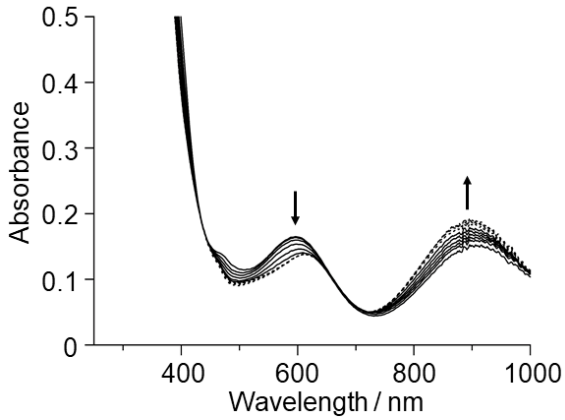

Figure 5. Spectral changes of [**3**]PF_6 in CH_2Cl_2 recorded after the stepwise addition of 0 - 1.0 eqs. (—) and 1.2 - 2.0 eqs. (····). No apparent changes were observed over the addition of a 1.0 eq. amount of CF_3SO_3H.

The reverse reaction for the protonated [**3**]PF_6 was not observed because of the immediate decomposition of the complex upon the addition of Me_4NOH. Complexes **1**, **2** and their oxidized forms were insensitive to the protonation under the same reaction conditions for **3** and [**3**]PF_6, consistent with the assumption that the PTA ligand uniquely serves a reactive site for **3** and [**3**]PF_6 with a proton. Taking these results together, **3** and [**3**]PF_6 react with a proton at one of six amino groups in the two axial PTA ligands and form mono-protonated species (**3**H^+ and [**3**H^+]PF_6, respectively) as the unique products of the reaction. Supportive data for the single protonation was obtained from EPR spectroscopy with [**3**]PF_6 in the presence of CF_3SO_3H (Figure S7). The spectral simulation required different A_{iso} values (1.45 and 2.05 mT) to fit the experimental data. This indicates that the unpaired electron in the central iron is non-equivalently delocalized over the two PTA ligands due to single protonation on one of the two ligands. Meanwhile, the total A_{iso} values for the two phosphorous atoms were found to be almost the same for [**3**]PF_6 (3.46 mT) and [**3**H^+]PF_6 (3.50 mT). Therefore, the protonation of [**3**]PF_6 did not change the total spin densities on the phosphorous atoms of the PTA ligands. DFT calculations

for [**3**]$^+$ and [**3**H$^+$]$^+$ reproduced this result and predicted an increase in the spin density on the nitrogen atom of the PTA ligand in [**3**H$^+$]PF_6 (*vide infra*). Indeed, the involvement of a nitrogen atom improved the fitting of the simulation to the experimentally obtained spectrum for [**3**H$^+$]PF_6 (Figure S7). The protonation raised the ν_{CO} energies of **3** and [**3**]PF_6 by ca. 20 cm^{-1} (Table 2, Figures S6b and d). This indicated that the protonation was effective in attenuating the π-backbonding from the central iron atom to the CO ligand, possibly due to a reduction of the electron-donating ability of the PTA ligand. As a result, the ν_{CO} energy of [**3**H$^+$]PF_6 surpassed that of [**2**]PF_6, which exhibits photosensitivity to the near-IR light for CO dissociation.[41]

The cyclic voltammogram obtained for **3** in CH_2Cl_2 shows major anodic and cathodic waves as a reversible couple with a midpoint potential of -340 mV (*vs.* Fc/Fc$^+$), corresponding to the one-electron oxidation of **3** (Figure 6).

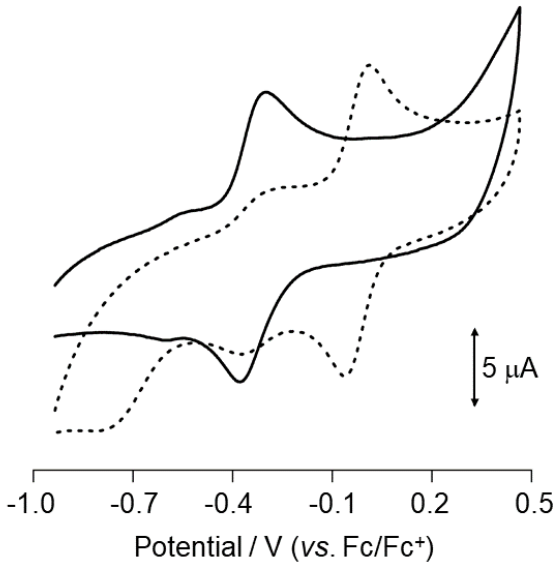

Figure 6. Cyclic voltammograms of **3** (—) and **3** in the presence of CF_3SO_3H (---) measured in CH_2Cl_2 containing 0.1 M ^{n}Bu$_4$NPF$_6$. WE, GC; CE, Pt wire; RE, Ag/Ag$^+$; Scan rate of 0.1 V s^{-1}. The potential was referred to as the redox couple of ferrocene/ferrocenium $E^{\circ\prime}$ (Fc/Fc$^+$).

When an equimolar amount of CF_3SO_3H with **3** was added to the electrolyte, the redox couple showed a positive shift by 300 mV except for the residual waves at the original potentials. Thus, the protonation biased the stability of the complex towards the reduced form (**3**) rather than the oxidized form ([**3**]$^+$). Since a redox potential is a thermodynamic parameter that depends on the relative stability of a compound in different oxidation states, the observed potential shift does not directly reflect changes in the electronic states of the central iron in **3** and [**3**]$^+$. Nevertheless, given the IR spectroscopy results, it is plausible to associate the positive shift in the potential with a decrease in the electron density of the central iron due to the attenuated electron-donating ability of the protonated PTA ligand.

3-3. Photoreaction of 3 and [3]PF$_6$. A previous study demonstrated that [**1**]PF_6 and [**2**]PF_6 undergo photolysis through the same reaction pathway (Scheme 1).[41]

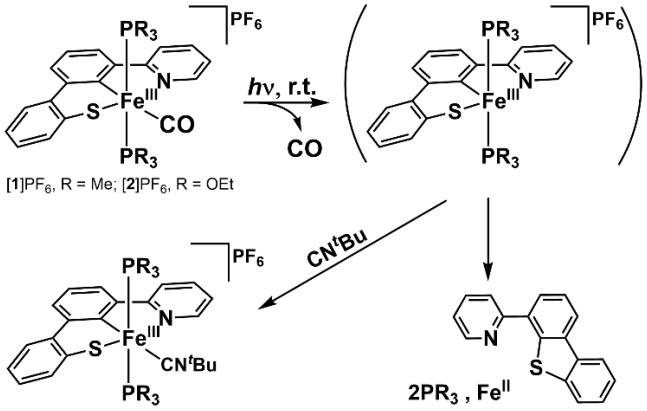

Scheme 1. Photolytic processes for [**1**]PF_6 and [**2**]PF_6 with CO dissociation.

The initial step in the photolysis is the dissociation of the CO ligand, which tentatively forms a penta-coordinated intermediate without removal or scrambling of ancillary ligands. This is supported by the fact that the photoreaction in the presence of isocyanide as a substituting ligand results in quantitative recovery of a hexa-coordinated species without the CO ligand. When the

substituting ligand is absent in the reaction mixture, the penta-coordinated intermediate rapidly disassembles to an equatorial ligand precursor, 4-(2'-pyridyl)dibenzothiophene (PyDBT), free phosphorous ligands, and iron ion (Fe^{II}) under ambient conditions. The disassembly step was confirmed by ^{1}H and $^{31}P\{^{1}H\}$ NMR spectroscopy and colorimetric detection of the iron(II) ion.[41] Gas chromatography was used to determine the stoichiometric amount of CO dissociated from [**1**]PF_6 and [**2**]PF_6, which excluded the reproduction of some iron-carbonyl compound after the disassembly step of the ancillary ligands.

The UV-Vis spectral changes observed for [**3**]PF_6 in CH_2Cl_2 upon light (λ = 400 nm) irradiation are shown in Figure 7.

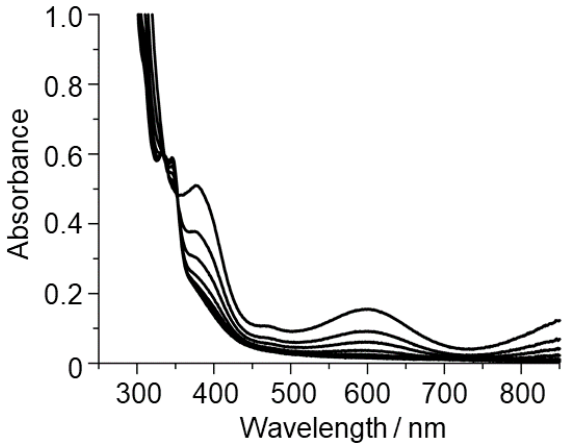

Figure 7. Time course of the photolysis of [**3**]PF_6 in CH_2Cl_2 upon irradiation with light (λ = 400 nm). The spectra were recorded every 15 min.

As observed for [**1**]PF_6 and [**2**]PF_6, the characteristic LMCT bands for [**3**]PF_6 disappear with isosbestic points at 334 and 352 nm; this concomitantly occurs with the emergence of a band at 346 nm, assignable to free PyDBT.[41] Mass spectrometry for the resultant solution found free PyDBT and the phosphorous monoxide of PTA as major photolytic products, which were also confirmed by NMR spectroscopy (Figure S8).

Colorimetric detection with phenanthroline revealed the quantitative effluence of free Fe^{II} for the reaction. The results confirmed that [**3**]PF_6 underwent photolysis via the same reaction pathway as [**1**]PF_6 and [**2**]PF_6 and that the kinetics for CO release were traceable via monitoring of the photolytic bleaching of the complex with UV-Vis spectroscopy. Analogous spectral changes were also observed for [**3**H^+]PF_6. The photolysis of [**3**]PF_6 and [**3**H^+]PF_6 at different light wavelengths was traced by monitoring the LMCT bands at 600 nm and 612 nm, respectively (Figures 8 and 9).

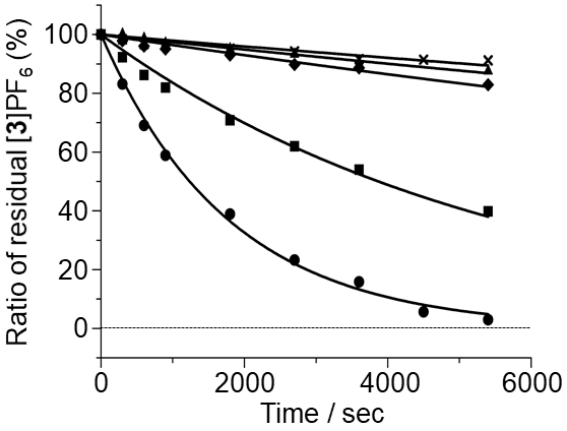

Figure 8. Photolysis kinetics of [**3**]PF_6 by irradiating with the light of different wavelengths in CH_2Cl_2 at room temperature. (●), 400 nm; (■), 450 nm; (◆), 500 nm; (▲), 600 nm; (X), in the dark. Each plot shows the average of three independent experimental results. The photolysis data obtained by light irradiation at wavelengths of 700 nm and 800 nm are omitted because of overlap with the data obtained in the dark. The experimental data at each light wavelength were analyzed with first-order kinetics by tracing the spectral changes at 600 nm (Figure S9).

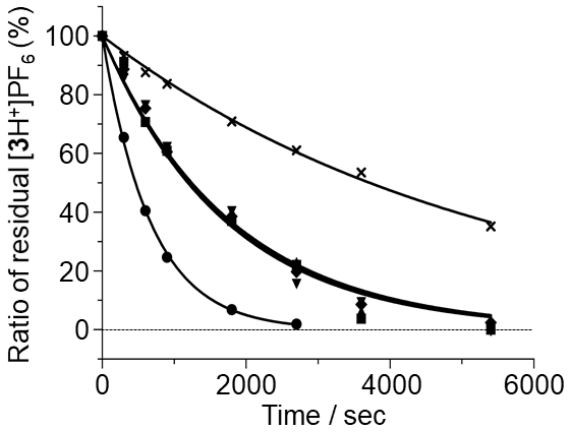

Figure 9. Photolysis kinetics of [**3**H$^+$]PF_6 by irradiating the light of different wavelengths in CH_2Cl_2 at room temperature. (●), 400 nm; (■), 500 nm; (◆), 600 nm; (▲), 700 nm; (▼), 800 nm; (X), in the dark. Each plot shows the average of three independent experimental results. The experimental data at each light wavelength were analyzed with first-order kinetics by tracing the spectral changes at 612 nm (Figure S10).

The photolysis rate constants for [**3**]PF_6 and [**3**H$^+$]PF_6 determined with first-order kinetics under the current experimental conditions are summarized in Table 3.

Wavelengths of light /nm	[**3**]PF_6	[**3**H$^+$]PF_6
400	5.6	1.5×10
450	1.8	n.d.
500	3.6×10^{-1}	5.8
600	2.6×10^{-1}	5.8
700	2.0×10^{-1}	5.8
800	2.0×10^{-1}	5.6
Dark	2.0×10^{-1}	1.9

Table 3. The rate constants ($/10^{-4}$ s^{-1}) for the photolysis of [**3**]PF_6 and [**3**H$^+$]PF_6 irradiated with different wavelengths of light.

As the photon flux density of the light source used in this study (Xenon light equipped in a fluorescent spectrometer) was approximately constant in the range of 500 nm and 800 nm (Figure S11), the kinetics data almost reflect the actual activity of [**3**]PF_6 and [**3**H^+]PF_6 on the photolysis by various wavelengths from visible to near-IR light. The photolysis of [**3**]PF_6 was observed when irradiated with light at wavelengths shorter than 500 nm. The obtained kinetics data was coincident with the photolytic properties of [**1**]PF_6. Meanwhile, the photolytic activity of [**3**H^+]PF_6 was analogous to that of [**2**]PF_6, which showed an invariable photolysis efficiency in the wavelength range of 500-800 nm, except for reduced thermal stability in the dark. The steric effect of single protonation on PTA was unlikely to distinguish the photolytic properties of [**3**]PF_6 and [**3**H^+]PF_6. Meanwhile, an apparent difference was found in the significant upward shift of the ν_{CO} energy for [**3**H^+]PF_6, reaching a value comparable to that obtained for [**2**]PF_6 (Table 2). Thus, the extended photosensitivity of [**3**H^+]PF_6 in the near-IR region should be attributed to the attenuated π-backbonding to CO due to the reduced electron-donation from the protonated PTA ligand to the central iron. The thermal instability of [**3**H^+]PF_6 in the dark implied that the attenuated π-backbonding to CO was no longer sufficient to stably retain the Fe-CO bond, leading to thermal dissociation of the CO ligand and subsequent disassembly of the complex. According to IR spectroscopy and the kinetic data, the current Fe^{III} carbonyl complexes with a ν_{CO} energy lower than 2000 cm^{-1} (**1** - **3**, [**1**]PF_6, and [**3**]PF_6) showed no photolytic activity with near-IR region light, while complexes with a ν_{CO} energy of over ca. 2010 cm^{-1} acquired near-IR light sensitivity in the photolysis ([**2**]PF_6, and [**3**H^+]PF_6). This is consistent with the photo-CO dissociation mechanism previously proposed for [**1**]PF_6 and [**2**]PF_6,[41] and suggests that the ν_{CO} energy is a useful index for tuning the photolytic sensitivity of the complexes towards near-IR light. The complex [**3**]PF_6 is a potential platform for dynamically turning on and

off the photo-CO dissociation by near-IR light in response to protonation of the PTA ligand. PTA derivatives with slightly enhanced electron-donating ability[45-47] are potential candidates for a ligand to improve the thermal stability of [**3**H$^+$]PF$_6$ while retaining photosensitivity to near-IR light.

3-4. DFT calculations. Quantum chemical calculations with density functional theory (DFT) at the uB3LYP/6-311+G(d,p) level were performed to confirm the effect of the protonation on the photosensitivity of [**3**H$^+$]PF$_6$. The optimized structure reproduced the crystal structure of **3** (Figure S12a) and was used to generate cationic moieties of [**3**]PF$_6$ and [**3**H$^+$]PF$_6$ ([**3**]$^+$ and [**3**H$^+$]$^+$). No apparent difference was observed in the structures of [**3**]$^+$ and [**3**H$^+$]$^+$ generated by the calculation (Figures S12b and c), consistent with the assumption that the protonated PTA ligand shows the little steric effect on the complex. The Mulliken atomic spin density at the central iron in [**3**H$^+$]$^+$ (0.600) was calculated to be smaller than that in [**3**]$^+$ (0.677) (Table S9). This was in line with the trend in the ability to donate electrons to CO ligands, as inferred from the IR data. The sums of spin densities on the two phosphorous atoms in [**3**]$^+$ and [**3**H$^+$]$^+$ were predicted to be 0.108 and 0.115, respectively. The marginal difference in these values is consistent with the EPR data: the sums of the A_{iso} values for phosphorous atoms in [**3**]$^+$ and [**3**H$^+$]$^+$ are almost invariant, irrespective of the protonation of the PTA ligand (*vide supra*). The calculation predicted an increase in overall spin densities on the nitrogen atoms of the PTA ligands in [**3**H$^+$]$^+$, indicating possible participation of the nitrogen atoms in receiving electrons from the central iron to reduce the bonding character of the Fe-CO bond in [**3**H$^+$]$^+$.

Photo-excitations in [**3**]$^+$ and [**3**H$^+$]$^+$ were calculated by using a time-dependent DFT (TD-DFT) method. The absorption spectra composed of the predicted photo-excitations are shown in Figure

10. The calculation data reasonably reproduced the overall features of the experimentally obtained spectra for [**3**]PF_6 and [**3**H^+]PF_6 (Figure 11).

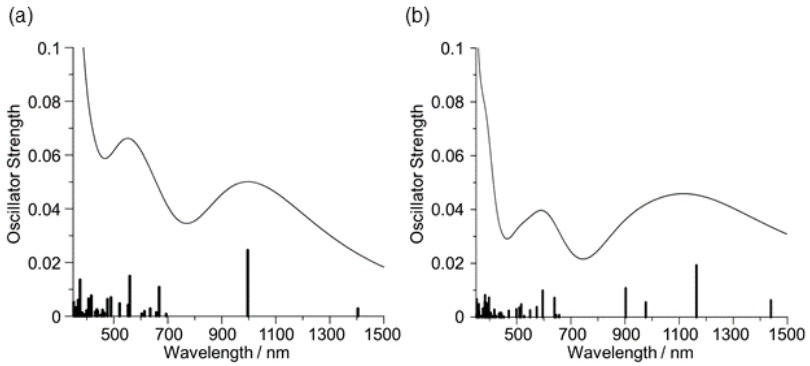

Figure 10. Oscillator strengths for photo-excitations predicted for **(**a) [**3**]$^+$ and (b) [**3**H^+]$^+$ by TD-DFT (TD = 100) at the uB3LYP/6-311+G(d,p) level (bar charts, see Tables S7 and 8). Solid lines show absorption spectra generated from the oscillator strengths.

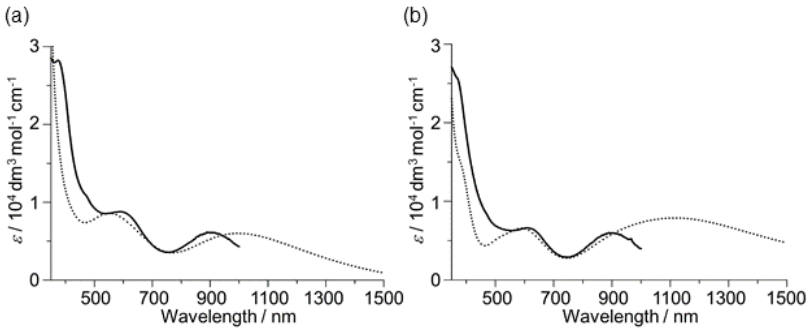

Figure 11. Comparison of experimental and generated absorption spectra for (a) [**3**]$^+$ and (b) [**3**H^+]$^+$. Solid lines show the experimental data measured in CH_2Cl_2. Dashed lines show the spectra reproduced from Figure 10.

An apparent discrepancy in the transitions between the experimental and calculated spectra was found in the near-IR region. This is a possible reflection of the strong charge-transfer character of the dominant excitations and the fact that their excitation energies tend to be underestimated in TD-DFT calculations.[56] Dominant molecular orbitals (MOs) associated with major photo-

excitations of [**3**]$^+$ and [**3**H$^+$]$^+$ at the longer wavelengths than 500 nm are listed in Tables 4 and 5, respectively.

Excitation light wavelength /nm		521	559	614	668	996	1403
Oscillation strength		0.0048	0.0150	0.0019	0.0109	0.0246	0.0029
MOs	Ground state	β-HOMO-7	α-HOMO	β-HOMO-8	β-HOMO-3	β-HOMO	β-HOMO-8
	Excited state	β-LUMO	α-LUMO	β-LUMO+3		β-LUMO	
Property of excitation		d-d	LMCT	d-d	LMCT	LMCT	d-d

Table 4. The dominant molecular orbitals for [**3**]$^+$ relevant to major photo-excitations generated by light with wavelengths longer than 500 nm. The shapes of the MOs are shown in Table S5.

Excitation light wavelength /nm		509	596	639	902	977	1164
Oscillation strength		0.0035	0.0098	0.0071	0.0107	0.0054	0.0192
MOs	Ground state	β-HOMO-7	α-HOMO-2	β-HOMO-4	β-HOMO-1	β-HOMO	β-HOMO-1
	Excited state	β-LUMO	α-LUMO		β-LUMO		
Property of excitation		d-d	LMCT	LMCT	LMCT	LMCT	LMCT

Excitation light wavelength /nm		1439
Oscillation strength		0.0062
MOs	Ground state	β-HOMO-6
	Excited state	β-LUMO
Property of excitation		d-d

Table 5. The dominant molecular orbitals for [**3**H$^+$]$^+$ associated with major photo-excitations generated by light with wavelengths longer than 500 nm. The shapes of the MOs are shown in Table S6.

The intense oscillators of [**3**]$^+$ and [**3**H$^+$]$^+$ in the near-IR region (996 and 1164 nm for [**3**]$^+$ and [**3**H$^+$]$^+$, respectively) were attributed to LMCT transitions from orbitals spread over the PTA or the biphenyl thiolate moiety of the PyBPT ligands to iron dπ orbitals (Tables S5 and 6). Other prominent oscillators were found around 600 nm (559 nm and 668 nm for [**3**]$^+$, 596 nm and 639 nm for [**3**H$^+$]$^+$), which were also assigned to LMCT transitions from the orbitals of the PTA and PyBPT ligands to the iron-centered dπ and dσ* orbitals. In a previous study, the corresponding transitions have been predicted for [**1**]$^+$ (1030, 568, and 555 nm) and [**2**]$^+$ (1087, 617, and 543 nm).[41] These LMCT transitions did not contribute to the photo-CO dissociation from the complexes, as the dominant molecular orbitals concerned with these transitions did not include the bonding or anti-bonding interactions of the Fe-CO bond. Meanwhile, as with [**1**]$^+$ and [**2**]$^+$, the TD-DFT calculation for [**3**]$^+$ and [**3**H$^+$]$^+$ predicted weak oscillators corresponding to d-d transitions behind the LMCT transitions in both the 500-600 nm wavelength range and the near-IR region. The ground states for the d-d transitions showed obvious π-bonding character between the iron and carbonyl ligand, and the excited states were found to be oriented perpendicular to the bonding. Thus, the d-d transitions could depopulate the Fe-CO π-bonding orbital and destabilize the coordination of CO. However, the photo-absorptions for the d-d transitions are suppressed due to the overlapping of the intense absorptions by the LMCT transitions and are, thus, rendered less efficient to induce the photoreaction. The protonation of the PTA ligand attenuated the π-backbonding from the central iron atom and induced the partial depopulation of the Fe-CO π-bonding orbitals. This compensated for the inefficient d-d transition to promote the destabilization and subsequent dissociation of the CO ligand in response to light with wavelengths longer than 500 nm. The scenario follows the mechanism previously proposed for CO dissociation from [**1**]$^+$ and [**2**]$^+$, while the steric homology of [**3**]$^+$ and [**3**H$^+$]$^+$ highlights the

electronic effect of the phosphorous ligands in modulating the photosensitivity of the current iron-carbonyl complexes to near-IR light.

4. Conclusion

In this study, we synthesized an iron(III) carbonyl complex with axial PTA ligands ([**3**]PF_6) to verify the mechanism of photo-CO dissociation from a series of *trans*-[Fe(PyBPT-κ^3*N,C,S*)(CO)$(PR_3)_2$]PF_6 complexes. The complex [**3**]PF_6 showed CO dissociation in response to light at wavelengths shorter than 500 nm, whereas single protonation at one of the PTA ligands extended the photosensitivity of the complex ([**3**H^+]PF_6) to the near-IR region. Spectroscopic and theoretical studies indicated that changes in the electron-donating ability of the PTA ligand in response to the protonation characterized the photo-CO dissociation from the complex. The results confirmed the photo-CO dissociation mechanism previously proposed for [**1**]PF_6 and [**2**]PF_6 and provided clues into a molecular design for dynamically adjusting the ranges of light wavelengths suitable for CO dissociation from *trans*-[Fe(PyBPT-κ^3*N,C,S*)(CO)$(PR_3)_2$]PF_6.

As expected from the solubility of free PTA in water, [**3**]PF_6 was soluble in buffer solutions with different pH levels. Although the thermal instability of [**3**H^+]PF_6 in the dark remains to be solved, [**3**]PF_6 is a potential candidate as a photoCORM that varies the light wavelength range of CO release depending on the pH of the dissolving medium. A preliminary experiment has found that [**3**]PF_6 is reasonably stable in an acidic buffer solution (pH 4) and shows photo-CO dissociation in response to near-IR light.

Acknowledgements

This study was supported by JSPS KAKENHI Grant Numbers JP 20K05543, and a Grant-in-Aid 2019 from the Koyanagi Research Foundation.

References

[1] L.K. Weaver, 'Carbon Monoxide Poisoning', *N. Engl. J. Med.* 360(12) (2009) 1217-1225. 10.1056/NEJMcp0808891

[2] R. Von Burg, 'Carbon monoxide', *J. Appl. Toxicol.* 19(5) (1999) 379-386.

[3] B. Widdop, 'Analysis of carbon monoxide', *Ann. Clin. Biochem.* 39 (2002) 378-391. 10.1258/000456302760042146

[4] G. Kikuchi, T. Yoshida, M. Noguchi, 'Heme oxygenase and heme degradation', *Biochem. Biophys. Res. Commun.* 338(1) (2005) 558-567. 10.1016/j.bbrc.2005.08.020

[5] L.E. Otterbein, M.P. Soares, K. Yamashita, F.H. Bach, 'Heme oxygenase-1: unleashing the protective properties of heme', *Trends Immunol.* 24(8) (2003) 449-455. 10.1016/s1471-4906(03)00181-9

[6] B. Wegiel, D.W. Hanto, L.E. Otterbein, 'The social network of carbon monoxide in medicine', *Trends Mol. Med.* 19(1) (2013) 3-11. 10.1016/j.molmed.2012.10.001

[7] I. Andreadou, E.K. Iliodromitis, T. Rassaf, R. Schulz, A. Papapetropoulos, P. Ferdinandy, 'The role of gasotransmitters NO, H_2S and CO in myocardial ischaemia/reperfusion injury and cardioprotection by preconditioning, postconditioning and remote conditioning', *Br. J. Pharmacol.* 172(6) (2015) 1587-1606. 10.1111/bph.12811

[8] B.E. Mann, R. Motterlini, 'CO and NO in medicine', *Chem. Commun.* (41) (2007) 4197-4208. 10.1039/b704873d

[9] R. Motterlini, L.E. Otterbein, 'The therapeutic potential of carbon monoxide', *Nat. Rev. Drug Discov.* 9(9) (2010) 728-U24. 10.1038/nrd3228

[10] S. Garcia-Gallego, G.J.L. Bernardes, 'Carbon-Monoxide-Releasing Molecules for the Delivery of Therapeutic CO In Vivo', *Angew. Chem.-Int. Edit.* 53(37) (2014) 9712-9721. 10.1002/anie.201311225

[11] D. Nguyen, C. Boyer, 'Macromolecular and Inorganic Nanomaterials Scaffolds for Carbon Monoxide Delivery: Recent Developments and Future Trends', *ACS Biomater. Sci. Eng.* 1(10) (2015) 895-913. 10.1021/acsbiomaterials.5b00230

[12] U. Schatzschneider, 'Photoactivated Biological Activity of Transition-Metal Complexes', *Eur. J. Inorg. Chem.* (10) (2010) 1451-1467. 10.1002/ejic.201000003

[13] S.H. Heinemann, T. Hoshi, M. Westerhausen, A. Schiller, 'Carbon monoxide - physiology, detection and controlled release', *Chem. Commun.* 50(28) (2014) 3644-3660. 10.1039/c3cc49196j

[14] M.A. Wright, J.A. Wright, 'PhotoCORMs: CO release moves into the visible', *Dalton Trans.* 45(16) (2016) 6801-6811. 10.1039/c5dt04849d

[15] T.R. Johnson, B.E. Mann, I.P. Teasdale, H. Adams, R. Foresti, C.J. Green, R. Motterlini, 'Metal carbonyls as pharmaceuticals? $Ru(CO)_3Cl(glycinate)$, a CO-releasing molecule with an extensive aqueous solution chemistry', *Dalton Trans.* (15) (2007) 1500-1508. 10.1039/b613629j

[16] F. Zobi, O. Blacque, 'Reactivity of $17e^-$ Complex $[(Re^{II}Br_4)Br(CO)_2]^{2-}$ with Bridging Aromatic Ligands. Characterization and CO-Releasing Properties', *Dalton Trans.* 40(18) (2011) 4994-5001. 10.1039/c1dt10110b

[17] F. Zobi, A. Degonda, M.C. Schaub, A.Y. Bogdanova, 'CO Releasing Properties and Cytoprotective Effect of *cis-trans*-$[Re^{II}(CO)_2Br_2L_2]^n$ Complexes', *Inorg. Chem.* 49(16) (2010) 7313-7322. 10.1021/ic100458j

[18] M.N. Pinto, I. Chakraborty, J. Jimenez, K. Murphy, J. Wenger, P.K. Mascharak, 'Therapeutic Potential of Two Visible Light Responsive Luminescent photoCORMs:

Enhanced Cellular Internalization Driven by Lipophilicity', *Inorg. Chem.* 58(21) (2019) 14522-14531. 10.1021/acs.inorgchem.9b02121
[19] B.E. Mann, 'CO-Releasing Molecules: A Personal View', *Organometallics* 31(16) (2012) 5728-5735. 10.1021/om300364a
[20] J.M. Dabrowski, B. Pucelik, A. Regiel-Futyra, M. Brindell, O. Mazuryk, A. Kyziol, G. Stochel, W. Macyk, L.G. Arnaut, 'Engineering of relevant photodynamic processes through structural modifications of metallotetrapyrrolic photosensitizers', *Coord. Chem. Rev.* 325 (2016) 67-101. 10.1016/j.ccr.2016.06.007
[21] U. Schatzschneider, 'Novel lead structures and activation mechanisms for CO-releasing molecules (CORMs)', *Br. J. Pharmacol.* 172(6) (2015) 1638-1650. 10.1111/bph.12688
[22] K. Ling, F. Men, W.C. Wang, Y.Q. Zhou, H.W. Zhang, D.W. Ye, 'Carbon Monoxide and Its Controlled Release: Therapeutic Application, Detection, and Development of Carbon Monoxide Releasing Molecules (CORMs)', *J. Med. Chem.* 61(7) (2018) 2611-2635. 10.1021/acs.jmedchem.6b01153
[23] U. Schatzschneider, 'PhotoCORMs: Light-triggered release of carbon monoxide from the coordination sphere of transition metal complexes for biological applications', *Inorg. Chim. Acta* 374(1) (2011) 19-23. 10.1016/j.ica.2011.02.068
[24] J. Jimenez, I. Chakraborty, S.J. Carrington, P.K. Mascharak, 'Light-triggered CO delivery by a water-soluble and biocompatible manganese photoCORM', *Dalton Trans.* 45(33) (2016) 13204-13213. 10.1039/c6dt01358a
[25] J. Jimenez, I. Chakraborty, A. Dominguez, J. Martinez-Gonzalez, W.M.C. Sameera, P.K. Mascharak, 'A Luminescent Manganese PhotoCORM for CO Delivery to Cellular Targets under the Control of Visible Light', *Inorg. Chem.* 57(4) (2018) 1766-1773. 10.1021/acs.inorgchem.7b02480
[26] E. Kottelat, A. Ruggi, F. Zobi, 'Red-light activated photoCORMs of Mn(I) species bearing electron deficient 2,2 '-azopyridines', *Dalton Trans.* 45(16) (2016) 6920-6927. 10.1039/c6dt00858e
[27] R. Mede, M. Klein, R.A. Claus, S. Krieck, S. Quickert, H. Gorls, U. Neugebauer, M. Schmitt, G. Gessner, S.H. Heinemann, J. Popp, M. Bauer, M. Westerhausen, 'CORM-EDE1: A Highly Water-Soluble and Nontoxic Manganese-Based photoCORM with a Biogenic Ligand Sphere', *Inorg. Chem.* 55(1) (2016) 104-113. 10.1021/acs.inorgchem.5b01904
[28] C. Nagel, S. McLean, R.K. Poole, H. Braunschweig, T. Kramer, U. Schatzschneider, 'Introducing $[Mn(CO)_3(tpa\text{-}\kappa^3N]^+$ as a novel photoactivatable CO-releasing molecule with well-defined iCORM intermediates - synthesis, spectroscopy, and antibacterial activity', *Dalton Trans.* 43(26) (2014) 9986-9997. 10.1039/c3dt51848e
[29] A.M. Mansour, O.R. Shehab, 'Experimental and quantum chemical calculations of novel photoactivatable manganese(I) tricarbonyl complexes', *J. Organomet. Chem.* 822 (2016) 91-99. 10.1016/j.jorganchem.2016.08.018
[30] M.J. Stout, A. Stefan, B.W. Skelton, A.N. Sobolev, M. Massi, A. Hochkoeppler, S. Stagni, P.V. Simpson, 'Synthesis and Photochemical Properties of Manganese(I) Tricarbonyl Diimine Complexes Bound to Tetrazolato Ligands', *Eur. J. Inorg. Chem.* 2020(3) (2020) 292-298. 10.1002/ejic.201900987
[31] D. Kalderon, B.L. Roberts, W.D. Richardson, A.E. Smith, 'A Short Amino-Acid Sequence Able to Specify Nuclear Location', *Cell* 39(3) (1984) 499-509. 10.1016/0092-8674(84)90457-4

[32] M.W. Hentze, M.U. Muckenthaler, B. Galy, C. Camaschella, 'Two to Tango: Regulation of Mammalian Iron Metabolism', *Cell* 142(1) (2010) 24-38. 10.1016/j.cell.2010.06.028
[33] M. Valko, K. Jomova, C.J. Rhodes, K. Kuca, K. Musilek, 'Redox- and non-redox-metal-induced formation of free radicals and their role in human disease', *Arch. Toxicol.* 90(1) (2016) 1-37. 10.1007/s00204-015-1579-5
[34] M. Farina, D.S. Avila, J.B.T. da Rocha, M. Aschner, 'Metals, oxidative stress and neurodegeneration: A focus on iron, manganese and mercury', *Neurochem. Int.* 62(5) (2013) 575-594. 10.1016/j.neuint.2012.12.006
[35] K. Jomova, M. Valko, 'Advances in metal-induced oxidative stress and human disease', *Toxicology* 283(2-3) (2011) 65-87. 10.1016/j.tox.2011.03.001
[36] R. Kretschmer, G. Gessner, H. Gorls, S.H. Heinemann, M. Westerhausen, 'Dicarbonyl-bis(cysteamine)iron(II) A light induced carbon monoxide releasing molecule based on iron (CORM-S1)', *J. Inorg. Biochem.* 105(1) (2011) 6-9. 10.1016/j.jinorgbio.2010.10.006
[37] W.P. Li, C.H. Su, L.C. Tsao, C.T. Chang, Y.P. Hsu, C.S. Yeh, 'Controllable CO Release Following Near Infrared Light-Induced Cleavage of Iron Carbonyl Derivatized Prussian Blue Nanoparticles for CO-Assisted Synergistic Treatment', *ACS Nano* 10(12) (2016) 11027-11036. 10.1021/acsnano.6b05858
[38] J. Ou, W.H. Zheng, Z.Y. Xiao, Y.P. Yan, X.J. Jiang, Y. Dou, R. Jiang, X.M. Liu, 'Core-shell materials bearing iron(II) carbonyl units and their CO-release via an upconversion process', *J. Mat. Chem. B* 5(41) (2017) 8161-8168. 10.1039/c7tb01434a
[39] H. Meyer, M. Brenner, S.P. Hofert, T.O. Knedel, P.C. Kunz, A.M. Schmidt, A. Hamacher, M.U. Kassack, C. Janiak, 'Synthesis of oxime-based CO-releasing molecules, CORMs and their immobilization on maghemite nanoparticles for magnetic-field induced CO release', *Dalton Trans.* 45(18) (2016) 7605-7615. 10.1039/c5dt04888e
[40] H. Meyer, F. Winkler, P. Kunz, A.M. Schmidt, A. Hamacher, M.U. Kassack, C. Janiak, 'Stabilizing Alginate Confinement and Polymer Coating of CO-Releasing Molecules Supported on Iron Oxide Nanoparticles To Trigger the CO Release by Magnetic Heating', *Inorg. Chem.* 54(23) (2015) 11236-11246. 10.1021/acs.inorgchem.5b01675
[41] T. Nakae, M. Hirotsu, H. Nakajima, 'CO Release from N,C,S-Pincer Iron(III) Carbonyl Complexes Induced by Visible-to-NIR Light Irradiation: Mechanistic Insight into Effects of Axial Phosphorus Ligands', *Inorg. Chem.* 57(14) (2018) 8615-8626. 10.1021/acs.inorgchem.8b01407
[42] C.A. Tolman, 'Electron Donor-Acceptor Properties of Phosphorus Ligands - Substituent Additivity', *J. Am. Chem. Soc.* 92(10) (1970) 2953-2956. 10.1021/ja00713a006
[43] A.L. Fernandez, C. Reyes, A. Prock, W.P. Giering, 'The stereoelectronic parameters of phosphites. The quantitative analysis of ligand effects (QALE)', *J. Chem. Soc.-Perkin Trans. 2* 5 (2000) 1033-1041.
[44] C.A. Tolman, 'Steric Effects of Phosphorus Ligands in Organometallic Chemistry and Homogeneous Catalysis', *Chem. Rev.* 77(3) (1977) 313-348. 10.1021/cr60307a002
[45] J. Bravo, S. Bolano, L. Gonsalvi, M. Peruzzini, 'Coordination chemistry of 1,3,5-triaza-7-phosphaadamantane (PTA) and derivatives. Part II. The quest for tailored ligands, complexes and related applications', *Coord. Chem. Rev.* 254(5-6) (2010) 555-607. 10.1016/j.ccr.2009.08.006
[46] A. Guerriero, M. Peruzzini, L. Gonsalvi, 'Coordination chemistry of 1,3,5-triaza-7-phosphatricyclo 3.3.1.1 decane (PTA) and derivatives. Part III. Variations on a theme:

Novel architectures, materials and applications', *Coord. Chem. Rev.* 355 (2018) 328-361. 10.1016/j.ccr.2017.09.024

[47] A.D. Phillips, L. Gonsalvi, A. Romerosa, F. Vizza, M. Peruzzini, 'Coordination chemistry of 1,3,5-triaza-7-phosphaadamantane (PTA) - Transition metal complexes and related catalytic, medicinal and photoluminescent applications', *Coord. Chem. Rev.* 248(11-12) (2004) 955-993. 10.1016/j.ccr.2004.03.010

[48] M. Hirotsu, K. Santo, C. Tsuboi, I. Kinoshita, 'Diiron Carbonyl Complexes Bearing an N,C,S-Pincer Ligand: Reactivity toward Phosphines, Heterolytic Fe-Fe Cleavage, and Electrocatalytic Proton Reduction', *Organometallics* 33(16) (2014) 4260-4268. 10.1021/om500558h

[49] R.A. Gaussian 09, M. J. Frisch, G. W. Trucks, H. B. Schlegel, G. E. Scuseria, M. A. Robb, J. R. Cheeseman, G. Scalmani, V. Barone, G. A. Petersson, H. Nakatsuji, X. Li, M. Caricato, A. Marenich, J. Bloino, B. G. Janesko, R. Gomperts, B. Mennucci, H. P. Hratchian, J. V. Ortiz, A. F. Izmaylov, J. L. Sonnenberg, D. Williams-Young, F. Ding, F. Lipparini, F. Egidi, J. Goings, B. Peng, A. Petrone, T. Henderson, D. Ranasinghe, V. G. Zakrzewski, J. Gao, N. Rega, G. Zheng, W. Liang, M. Hada, M. Ehara, K. Toyota, R. Fukuda, J. Hasegawa, M. Ishida, T. Nakajima, Y. Honda, O. Kitao, H. Nakai, T. Vreven, K. Throssell, J. A. Montgomery, Jr., J. E. Peralta, F. Ogliaro, M. Bearpark, J. J. Heyd, E. Brothers, K. N. Kudin, V. N. Staroverov, T. Keith, R. Kobayashi, J. Normand, K. Raghavachari, A. Rendell, J. C. Burant, S. S. Iyengar, J. Tomasi, M. Cossi, J. M. Millam, M. Klene, C. Adamo, R. Cammi, J. W. Ochterski, R. L. Martin, K. Morokuma, O. Farkas, J. B. Foresman, and D. J. Fox, Gaussian, Inc., Wallingford CT, 'Gaussian 09, Revision A.02, M. J. Frisch, G. W. Trucks, H. B. Schlegel, G. E. Scuseria, M. A. Robb, J. R. Cheeseman, G. Scalmani, V. Barone, G. A. Petersson, H. Nakatsuji, X. Li, M. Caricato, A. Marenich, J. Bloino, B. G. Janesko, R. Gomperts, B. Mennucci, H. P. Hratchian, J. V. Ortiz, A. F. Izmaylov, J. L. Sonnenberg, D. Williams-Young, F. Ding, F. Lipparini, F. Egidi, J. Goings, B. Peng, A. Petrone, T. Henderson, D. Ranasinghe, V. G. Zakrzewski, J. Gao, N. Rega, G. Zheng, W. Liang, M. Hada, M. Ehara, K. Toyota, R. Fukuda, J. Hasegawa, M. Ishida, T. Nakajima, Y. Honda, O. Kitao, H. Nakai, T. Vreven, K. Throssell, J. A. Montgomery, Jr., J. E. Peralta, F. Ogliaro, M. Bearpark, J. J. Heyd, E. Brothers, K. N. Kudin, V. N. Staroverov, T. Keith, R. Kobayashi, J. Normand, K. Raghavachari, A. Rendell, J. C. Burant, S. S. Iyengar, J. Tomasi, M. Cossi, J. M. Millam, M. Klene, C. Adamo, R. Cammi, J. W. Ochterski, R. L. Martin, K. Morokuma, O. Farkas, J. B. Foresman, and D. J. Fox, Gaussian, Inc., Wallingford CT, 2016.', (2016).

[50] L.J. Farrugia, 'WinGX and ORTEP for Windows: an update', *J. Appl. Crystallogr.* 45 (2012) 849-854. 10.1107/s0021889812029111

[51] A. Altomare, M.C. Burla, M. Camalli, G.L. Cascarano, C. Giacovazzo, A. Guagliardi, A.G.G. Moliterni, G. Polidori, R. Spagna, 'SIR97: a new tool for crystal structure determination and refinement', *J. Appl. Crystallogr.* 32 (1999) 115-119. 10.1107/s0021889898007717

[52] G.M. Sheldrick, 'Crystal structure refinement with SHELXL', *Acta Crystallogr. Sect. C-Struct. Chem.* 71 (2015) 3-8. 10.1107/s2053229614024218

[53] T. Nakae, M. Hirotsu, I. Kinoshita, 'Di- and Mononuclear Iron Complexes of N,C,S-Tridentate Ligands Containing an Aminopyridyl Group: Effect of the Pendant Amine Site on Catalytic Properties for Proton Reduction', *Organometallics* 34(16) (2015) 3988-3997. 10.1021/acs.organomet.5b00366

[54] T. Nakae, M. Hirotsu, S. Aono, H. Nakajima, 'Visible-light-induced release of CO by thiolate iron(III) carbonyl complexes bearing N,C,S-pincer ligands', *Dalton Trans.* 45(41) (2016) 16153-16156. 10.1039/c6dt03399g
[55] D.J. Darensbourg, J.B. Robertson, D.L. Larkins, J.H. Reibenspies, 'Water-soluble organometallic compounds. 7. Further studies of 1,3,5-triaza-7-phosphaadamantane derivatives of group 10 metals, including metal carbonyls and hydrides', *Inorg. Chem.* 38(10) (1999) 2473-2481. 10.1021/ic981243j
[56] T.A. Niehaus, T. Hofbeck, H. Yersin, 'Charge-transfer excited states in phosphorescent organo-transition metal compounds: a difficult case for time dependent density functional theory?', *RSC Adv.* 5(78) (2015) 63318-63329. 10.1039/c5ra12962a